

NANOPHYSICS LABORATORY REPORT

Synthesis and characterization of gold nanoparticles

PHYSICS DEGREE Academic Year 2021-2022

Bogoni Enrico
Cicioni Rachele
Di Spena Maria Sharon

June 15, 2022

Abstract

The aim of the experience is to do the optical characterization of the gold nanoparticles. First the nanoparticles were chemically synthesized. Then we made a measurement of absorbance with the spectrophotometer from which we made an analysis of the optical properties in dipolar approximation. Subsequently, through X-ray diffraction, we obtained a measurement of the diameter of the nanoparticles. Finally, the shape and size of these nanoparticles was verified with electronic microscopy.

1. Chemical Synthesis

The method used for the synthesis of gold nanoparticles is the *Turkevich method*, developed by John Turkevich. This method is based on the reduction in aqueous solution of tetrachloroauric acid HAuCl_4 by sodium citrate $\text{Na}_3\text{C}_6\text{H}_5\text{O}_7$, at high temperatures. Sodium citrate, in addition to decompose tetrachloroauric acid, also controls the growth of nanoparticles due to the shielding effect of citrate anions. Therefore by controlling the concentration of the two elements, we can control the size of the nanoparticles. The procedure consisted of pouring 9.5 ml of aqueous solution of HAuCl_4 into a beaker and covered with a watch glass. The beaker is partially immersed in the crystallizer filled with tap water brought to 100°C. Then the stirrer is activated, ensuring the homogeneity of temperature and concentration of the tetrachloroauric acid. The sodium citrate solution is separately heated up to 100°C and 0.5 ml of HAuCl_4 are placed in the beaker. The solution has been left for 15 minutes at 100°C with the stirrer activated. In a few seconds the color of the solution change from yellow to dark red. In this way we obtain a ratio 5:1 between the citrate and the gold.

2. Optical Spectroscopy

The solution with nanoparticles obtained in the previous steps is diluted to obtain 95 μM concentration. Subsequently 0.3 ml of nanoparticles solution are added to 2.7 ml ultrapure water in a plastic cuvettes with an optical path z of 1 cm.

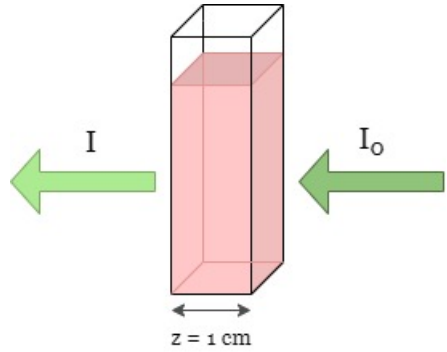


Figure 1: Schematization of the Lambert-Beer experiment.

For the optical characterization of the sample, the Lambert-Beer experiment is reproduced using the Jasco V670 Spectrophotometer. A monochromatic wave passes through the sample from which the attenuated beam re-emerges in a collinear direction with the incoming beam, as shown in the **Figure 1**. The wavelength of the incoming beam varies from 400 nm to 800 nm with a step of 1 nm. The attenuation of the incoming beam is described by *Lambert-Beer's law*:

$$I(z) = I_0 e^{-\gamma z}$$

where γ is the attenuation coefficient and z is the length of the sample in the direction of the beam, i.e. the optical path of the cuvette. The two physical quantities of interest are the transmittance T and the absorbance A :

$$T = \frac{I(z)}{I_0}$$

$$A = \log_{10} \frac{1}{T} = \gamma z \log_{10}(e) = \rho \sigma_{ext} z \log_{10}(e)$$

where ρ is the volumetric density of nanoparticles and σ_{ext} the extinction cross section. The experimental curve obtained through the software in the laboratory is the absorbance curve $A_{exp}(\lambda)$, as a function of the wavelength, and it is shown in the **Figure 2**. As can be seen the characteristic SPR peak is present for $\lambda_{peak} = 528\text{nm}$.

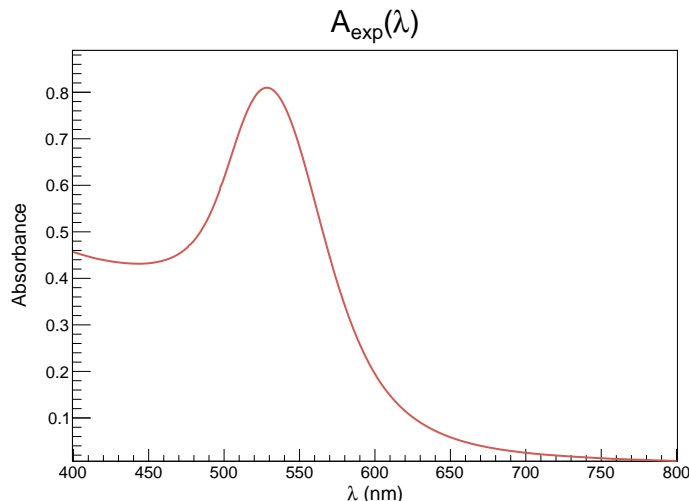


Figure 2: Experimental absorbance.

To obtain information about the characteristics of nanoparticles we will use the Mie theory in dipolar approximation. This means that we impose some hypothesis for the system under examination:

- the nanoparticles are considered spherical¹ with radius R;
- the medium in which they are located (water) is considered non-absorbent, therefore the dielectric function ε_m of the medium is real;
- in the dipolar approximation the nanoparticles are non-interacting and it's valid the condition $R \ll \lambda$.

The absorbance depends on the extinction cross section σ_{ext} which, in the dipolar approximation, is given by the *Mie formula*:

$$\sigma_{ext} = 9 \frac{2\pi}{\lambda} \varepsilon_m^{3/2} \frac{4}{3} \pi R^3 \frac{\varepsilon_2}{(\varepsilon_1 + 2\varepsilon_m)^2 + (\varepsilon_2)^2}$$

Therefore:

$$A = \rho z \log_{10}(e) 9 \frac{2\pi}{\lambda} \varepsilon_m^{3/2} \frac{4}{3} \pi R^3 \frac{\varepsilon_2}{(\varepsilon_1 + 2\varepsilon_m)^2 + (\varepsilon_2)^2}$$

where $\varepsilon_1 = \varepsilon_1(\omega)$ and $\varepsilon_2 = \varepsilon_2(\omega)$ are respectively the real and imaginary part of the dielectric function of gold $\varepsilon(\omega) = \varepsilon_1(\omega) + i\varepsilon_2(\omega)$.

The purpose of our analysis is to find the absorbance $A(R, \rho, \varepsilon_m)$ that best approximates the experimental curve; in this way it's possible to obtain the best values for R, ρ and ε_m .

It is possible to make a further correction for ε_1 and ε_2 which consists in the following size correction:

$$\begin{aligned} \varepsilon_1(\omega, R) &= \varepsilon_1(\infty) + \omega_p^2 \left(\frac{1}{\omega^2 + \Gamma_\infty^2} - \frac{1}{\omega^2 + \Gamma(R)^2} \right) \\ \varepsilon_2(\omega, R) &= \varepsilon_2(\infty) - \frac{\omega_p^2}{\omega^2 + \Gamma_\infty^2} \left(\frac{\Gamma_\infty}{\omega^2 + \Gamma_\infty^2} - \frac{\Gamma(R)}{\omega^2 + \Gamma(R)^2} \right) \end{aligned}$$

where the bulk plasmon frequency is $\omega_p = 1.37 \cdot 10^{16}$ Hz and the bulk relaxation frequency is $\Gamma_\infty = 1.08 \cdot 10^{14}$ Hz. The relaxation frequency as a function of R is $\Gamma(R) = \Gamma_\infty + \frac{\pi v_F}{4R}$ where the Fermi velocity is $v_F = 1.4 \cdot 10^6$ m/s. The **Figure 3** shows the trend of the two functions $\varepsilon_1(\omega, R)$, $\varepsilon_2(\omega, R)$ as a function of R and λ .

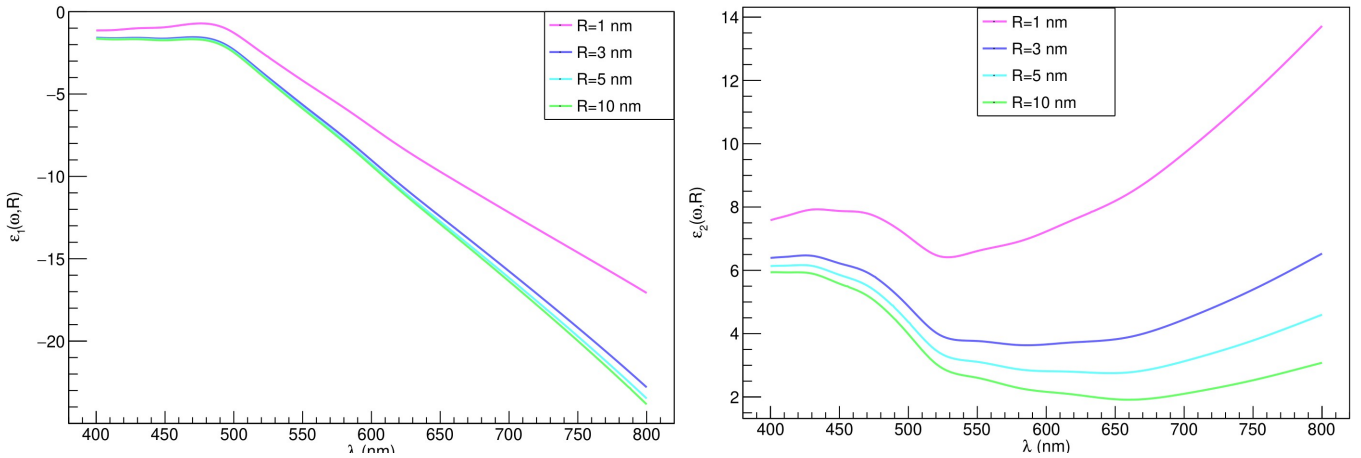


Figure 3: Real and imaginary part of the dielectric function of gold with size correction.

¹This hypothesis will be discussed in the **paragraph 5**.

In order to obtain the best fit for the absorbance we consider only the data around the peak and so the range for the wavelength considered is [460,580] nm. The quantitative parameter used to evaluate the fits is the χ^2 defined as follows:

$$\chi^2 = \sum_{\lambda_i} \frac{(A_{exp} - A_{fit})^2}{\frac{1}{A_{exp}}}$$

in which the statistical weight $\frac{1}{A_{exp}}$ is chosen to give greater weight to the values of the absorbance around the peak. The lower the value of χ^2 , the better the A_{fit} curve considered. The parameters that vary in the A_{fit} are R , ρ and ε_m .

Initially one of the three parameters is fixed while the other two vary.

First we set the value of $\varepsilon_m \equiv \varepsilon_m^{Frohlich}$ while the parameters (R, ρ) vary. The $\varepsilon_m^{Frohlich}$ value is obtained from the value of λ_{peak} , using the Frohlich condition: $\varepsilon_1 + 2\varepsilon_m = 0$. The range of variation of R is [3.00, 8.00] nm, while the range of ρ is $[10^{-11}, 1000 \cdot 10^{-11}] nm^{-3}$. For each triplets $(R, \rho, \varepsilon_m^{Frohlich})$ we have a value of χ^2 and at the end of the cycle the program used gives the values $(R^*, \rho^*, \varepsilon_m^{Frohlich})$ which minimize the χ^2 .

Then we consider the couple (R, ε_m) fixing the ρ^* obtained from the previous cycle. The radius varies in the same range as before while the range of variation of ε_m is [1.30, 2.80]. The two iterations are done with and without size correction for the dielectric function. The **Figure 4** shows the trend of the χ^2 in the two cycles without the size correction. It can be seen that R and ρ are correlated quantities because the minimum basin for χ^2 is not localized but there is a continuous curve. On the other hand, for the couple (R, ε_m) the basin of minimum is more localized, which allows us to narrow the range of variation of ε_m .

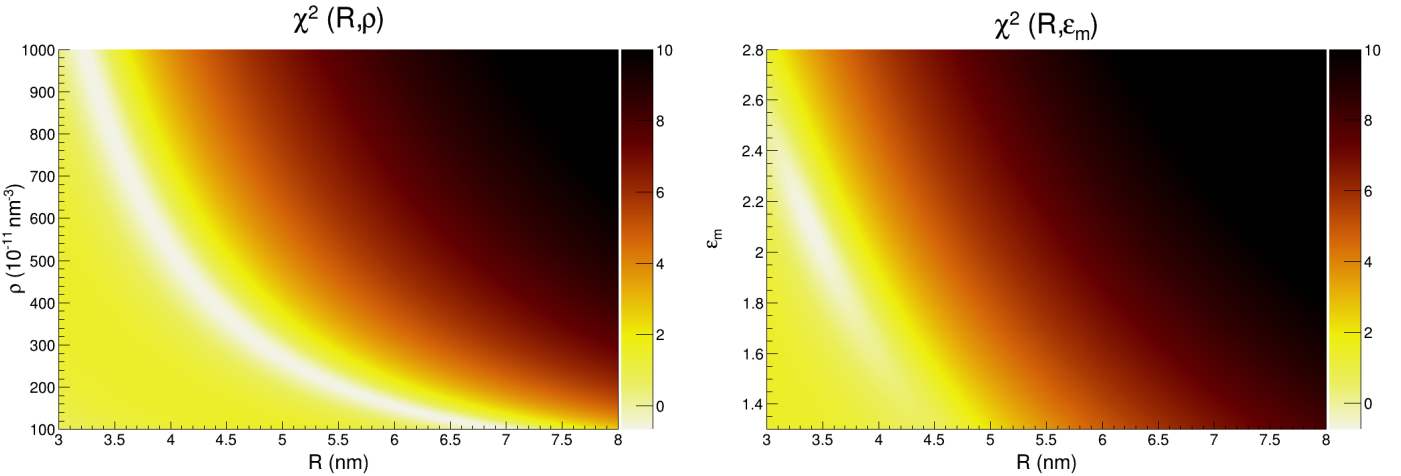


Figure 4: Plot 2D of χ^2 without the size correction in logarithmic scale.

The **Figure 5** shows the same graphs with size correction. It is clear that the basins are more defined. For a quantitative comparison the **Table 1** and **Table 2** show the values relating to the minimum of χ^2 for the two cycle and for both cases (with and without size correction S.C.).

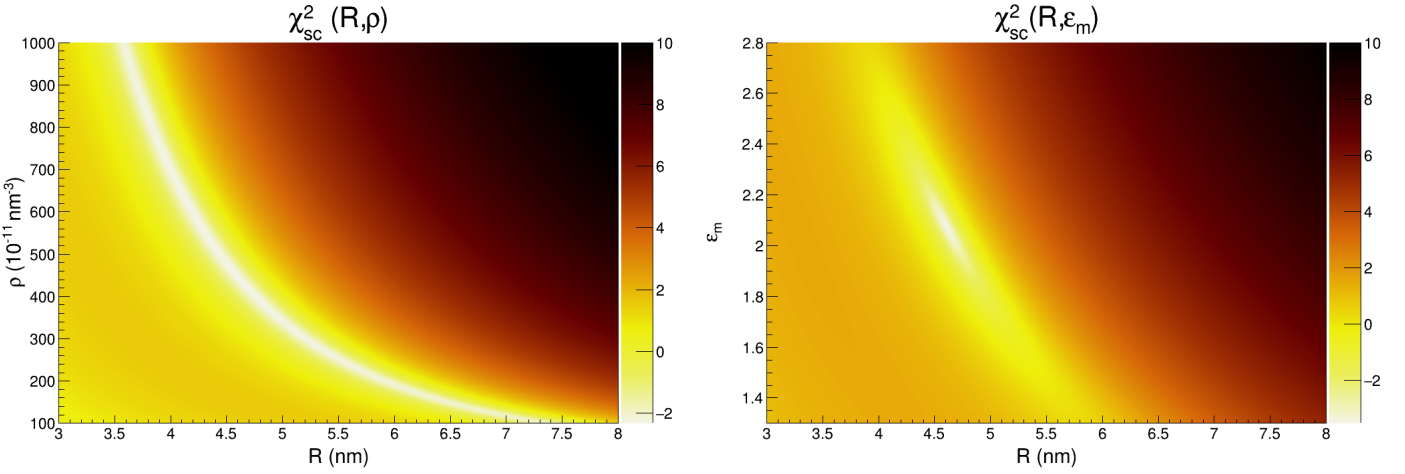


Figure 5: Plot 2D of χ^2 with the size correction in logarithmic scale.

	$R^*(\text{nm})$	$\rho^*(\text{nm}^{-3})$	χ^2
Without S.C.	3.27	$9.57 \cdot 10^{-9}$	0.515
With S.C.	4.44	$4.98 \cdot 10^{-9}$	0.097

Table 1: Values of R^* and ρ^* with the minimum χ^2 .

	$R^*(\text{nm})$	ε_m^*	χ^2
Without S.C.	3.38	2.10	0.471
With S.C.	4.60	2.07	0.097

Table 2: Values of R^* and ε_m^* with the minimum χ^2 .

Since the value of χ^2 is better with the size correction, from now on we will consider them.

In **Figure 6** we can compare the experimental absorbance A_{exp} with the absorbances $A_{SC}(R^*, \rho^*)$ and $A_{SC}(R^*, \varepsilon_m^*)$, with size corrections. As shown, even if we have considered the values that minimize the χ^2 , the curves obtained do not come very close to the experimental curve.

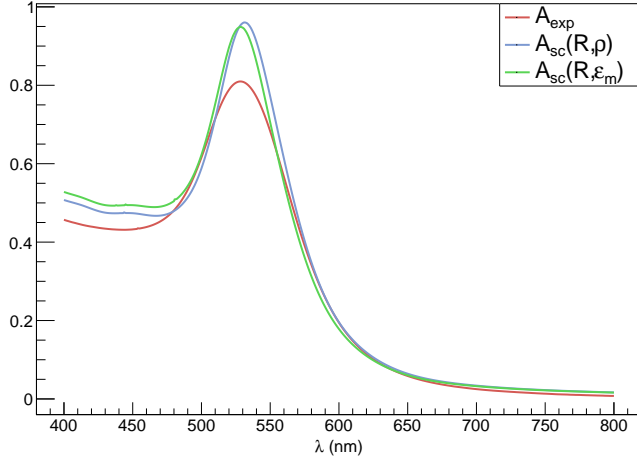


Figure 6: Comparison between the experimental absorbance and the absorbances obtained by varying the pairs (R, ρ) and (R, ε_m) .

For this reason we decide to vary the three parameters at the same time. The ranges of variation of R and ρ don't change because, as shown in **Figure 3, 4**, no minimum basin is identified for the χ^2 . Instead for ε_m it is possible to narrow the range that becomes $[1.80, 2.50]$. The values of the three parameters obtained with the simultaneous variation of them are shown in **Table 3**. The

$R(\text{nm})$	$\rho(\text{nm}^{-3})$	ε_m	χ^2
4.0 ± 0.2	$(8 \pm 1) \cdot 10^{-11}$	2.1 ± 0.2	0.024

Table 3: The final value of R , ρ and ε_m for the optical spectroscopy.

error on the values are taken considered a threshold value for the χ^2 .

In **Figure 7** is shown the absorbance (with size correction) obtained with the values of **Table 3**.

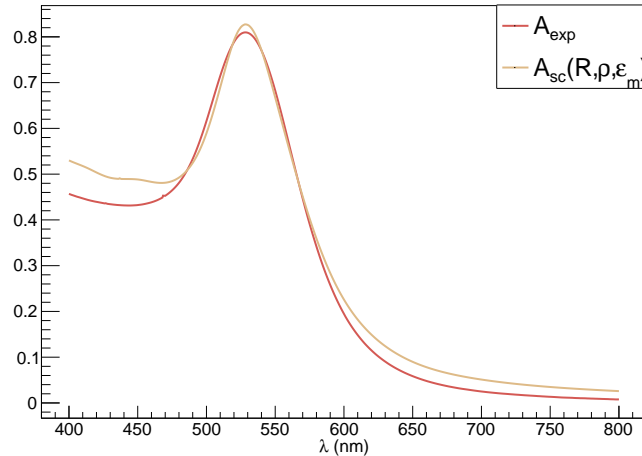


Figure 7: The experimental absorbance A_{exp} and the absorbance with the final value of R , ρ and ε_m .

2.1. Comments

Looking at the results of the tables it can be seen that with the size corrections there is a better agreement, i.e. a minor χ^2 , as expected.

As can be seen from the plot 2D of χ^2 the variables R and ρ are strongly correlated; this is due to the fact that in the expression of σ_{ext} there is the product between ρ and R^3 . Given this correlation, the value of ρ^* obtained in the first iteration is not reliable. In fact, observing the absorbance curves in **Figure 6**, we can think that the minimum basin in which our quantities have stabilized is not the correct minimum basin. For this reason we preferred to proceed with the iteration of all three variables, which also gave us better results for χ^2 , as we expected.

Observing **Figure 7** we see that in the interband region there is a gap between the curves which could mean that the radius obtained could be underestimated. In this first part of the experience we are making stringent assumptions about the system and therefore the obtained value of the radius is really approximate, therefore we expect different results in the following parts of the experience. At last the value of ε_m gives us a refractive index $n \approx 1.43$ which differs from that of water. This may be due to the fact that after the synthesis of gold nanoparticles in water remain some anions coming from the precursor that modify the refractive index of pure water ($n=1.33$).

3. X-ray Diffraction Analysis

As XRD aim is the analysis of crystalline structure, gold nanoparticles need to be placed similarly to a solid state configuration. To do so we fix with the APTES compound the nanoparticles on a substrate of monocrystalline sample of silica. X-rays are produced using a Cu source of wavelength $\lambda = 0.15406\text{nm}$. We collect the intensities of the beams diffracted by the sample of gold nanoparticles at angles 2θ with respect to the incident beam, using the X-ray diffractometer X'Pert PRO. We keep the incidence angle fixed at a grazing incidence of $\omega = 0.6^\circ$ with respect to the horizontal plane, in order to obtain information only from the surface of the sample, as to mainly probe the nanoparticles, and to improve the signal-to-noise ratio. In **Figure 8** it is showed the experimental intensity of diffracted beams by gold nanoparticles.

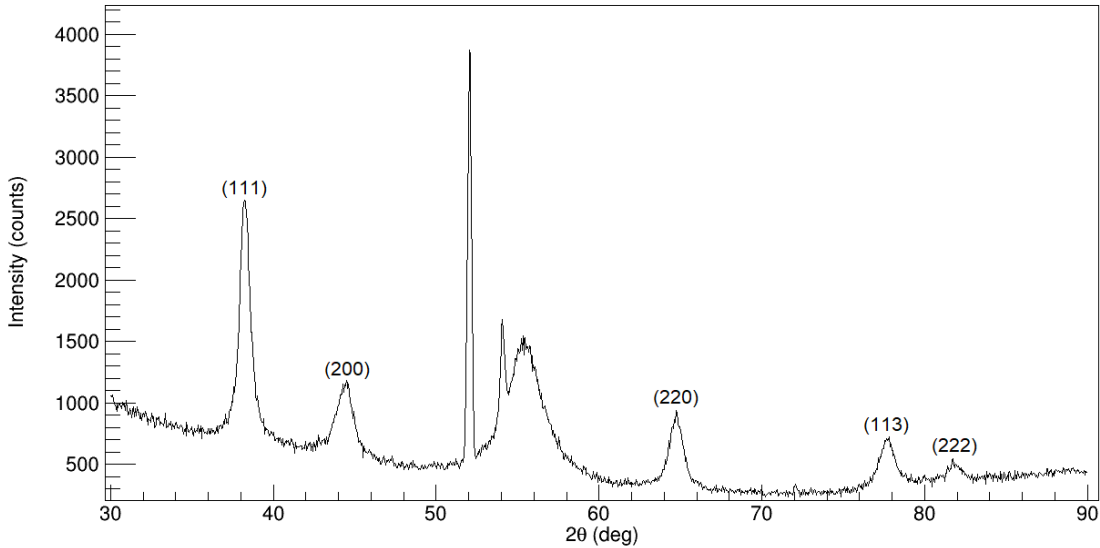


Figure 8: Experimental intensity of diffracted beams by gold nanoparticles as a function of the angle 2θ . The peaks are labeled with the respective Miller indexes for f.c.c. structure.

To assign the Miller indexes to each gold NPs peak we assume the f.c.c. structure for the crystal, as it's the one of bulk gold crystals, disregarding the peaks in the range $[50^\circ, 60^\circ]$ belonging to the silica substrate. To measure the centroid, the height and the FWHM of the peaks, we fit them with a sum of a linear function for the background noise and a pseudo-Voigt function for the effective signal. The pseudo-Voigt distribution is a linear combination of a Gaussian and a Lorentzian distribution with shared Amplitude, centroid and FWHM, defined as:

$$pV(x; A, \mu, \Gamma, \alpha) = A \left(\frac{\alpha}{\Gamma} \sqrt{\frac{4 \ln 2}{\pi}} \exp \left\{ -\frac{1}{2} \left(\frac{(x - \mu)\sqrt{8 \ln 2}}{\Gamma} \right)^2 \right\} + \frac{(1 - \alpha)}{\pi} \left[\frac{\Gamma/2}{(x - \mu)^2 + (\Gamma/2)^2} \right] \right)$$

with amplitude A , centroid μ , FWHM Γ and α , a mixing parameter to control the relative weight of Gaussian and Lorentzian components, with $0 \leq \alpha \leq 1$. In **Figure 9** can be seen the graphs of the five fitted peaks.

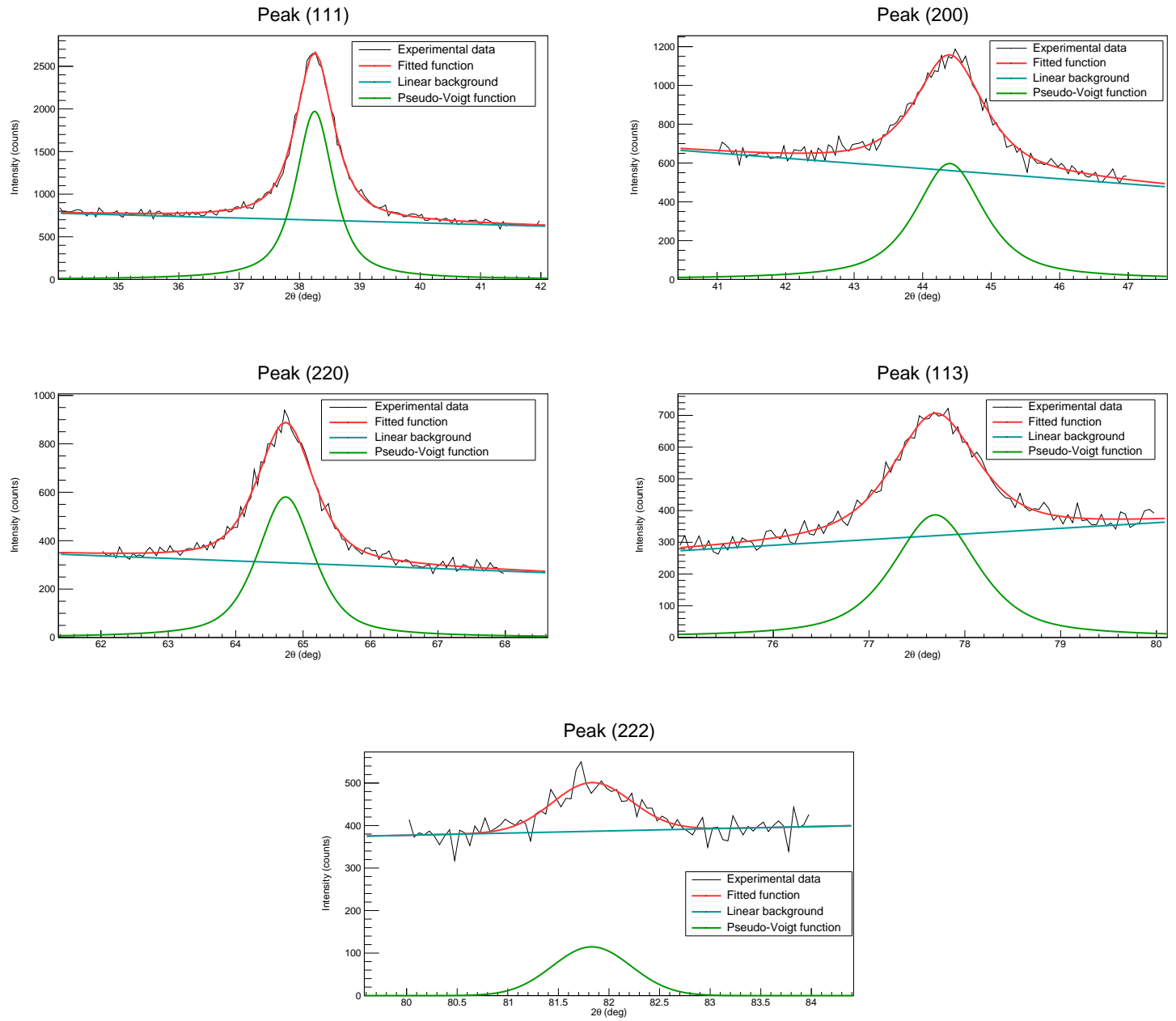


Figure 9: Fit of the experimental data in correspondence to the gold peaks. In red the fitted function, in blue the contribute of the linear background and in green the pseudo-Voigt function.

We verify the assumption of f.c.c. structure and the correctness of the indexes given to the different peaks by computing the gold lattice parameter a , and comparing it with the bulk one $a_{bulk} = 0.408$ nm. To do this, from the *Bragg's law* and the relation between inter-planar spacing and the lattice parameter, we calculate the latter for each peak:

$$a = \frac{\lambda}{2 \sin \theta} \cdot (h^2 + k^2 + l^2)^{1/2}$$

where θ and h, k, l are respectively the angle (in radians) and the three Miller indexes corresponding to each peak.

In the **Table 4** we report the results for the peaks fit parameters and for the lattice constant.

M.I.	Centroid (2θ) (rad)	FWHM (rad)	α	a (nm)
(111)	0.66760 ± 0.00004	0.0129 ± 0.0002	0.20 ± 0.03	0.40722 ± 0.00003
(200)	0.7749 ± 0.0002	0.0209 ± 0.0006	0.2 ± 0.1	0.40774 ± 0.00008
(220)	1.1299 ± 0.0001	0.0173 ± 0.0003	0.32 ± 0.07	0.40695 ± 0.00003
(113)	1.3560 ± 0.0001	0.0184 ± 0.0006	0.3 ± 0.1	0.40732 ± 0.00004
(222)	1.4282 ± 0.0005	0.016 ± 0.001	1.0 ± 0.3	0.4074 ± 0.0001

Table 4: Values obtained for the main pseudo-Voigt fit parameters and for the lattice constant a .

Its error is computed by the error propagation as:

$$\sigma_a = \frac{\lambda \cos \theta}{2 \sin^2 \theta} \cdot (h^2 + k^2 + l^2)^{1/2} \cdot \sigma_\theta$$

We use the *Scherrer equation* to calculate the size of the nanoparticles in the direction of the planes that produce the diffraction peaks. It relates the peak broadening β to the volume-weighted crystallite size in the following way:

$$D_V = K \frac{\lambda}{\beta \cos \theta}$$

The broadening β can be defined in two different ways:

- as the FWHM of the peak ($\beta_{FWHM} = \Gamma$);
- as the integral breadth ($\beta_{breadth}$) of a reflection located at 2θ , defined as area of the peak divided by its height.

The parameter K is the Scherrer constant which depends on the shape and on the way of measurement of the broadening. For spherical nanoparticles it's set equal to 1.07 rad for $\beta_{breadth}$ and 0.89 rad for β_{FWHM} .

The observed broadening β_{obs} that we compute from the peaks data it's the result of two different contributes: the size broadening β_{size} that enters in the Scherrer equation, and the instrumental broadening β_{inst} due to the not perfectly collimated incident beam. Since the latter contribution has been already measured for the diffractometer with a monochromatic source as $\beta_{inst} = 0.27^\circ$ we can easily calculate β_{size} in two different ways:

$$\begin{aligned} \beta'_{size} &= \sqrt{\beta_{obs}^2 - \beta_{inst}^2} \\ \beta''_{size} &= \beta_{obs} - \beta_{inst} \end{aligned}$$

In **Table 5** we report the values for the size broadenings and the crystallite size for each peak. The prime and double prime symbols distinguish the method of calculations of β_{size} .

M.I.	D'_{VFWHM} (nm)	D''_{VFWHM} (nm)	$D'_{Vbreadth}$ (nm)
(111)	12.0 ± 0.2	17.6 ± 0.3	10.1
(200)	7.3 ± 0.2	9.2 ± 0.3	6.4
(220)	9.7 ± 0.2	12.9 ± 0.3	8.8
(113)	9.9 ± 0.3	12.8 ± 0.5	8.8
(222)	12 ± 1	16 ± 2	13.4

Table 5: Experimental results of crystallite size for each peak obtained with different methods.

The error associated to D_V is computed by the error propagation as:

$$\sigma_{D_V} = K\lambda \sqrt{\left(\frac{1}{\beta_{size}^2 \cos \theta}\right)^2 \sigma_{\beta_{size}}^2 + \left(\frac{\sin \theta}{\beta_{size} \cos^2 \theta}\right)^2 \sigma_\theta^2}$$

where σ_θ is the error associated to the centroid parameter by the fit. We decide to calculate the $\beta_{breadth}$ only to verify the same trend seen with the β_{FWHM} in the size values of the nanoparticles from one family of planes to another.

We also try to apply the Williamson-Hall analysis to take in account the possible contribution of the strain broadening by solving the following equation with a linear fit of our data, but the small number of diffraction peaks gives us a huge radius ($> 50\text{nm}$) so we don't use this type of analysis.

$$\beta_{size} \cos \theta = K \frac{\lambda}{D_V} + 4\epsilon_{str} \sin \theta$$

3.1. Comments

As can be seen in the results of **Table 4**, we verified correctly the assumption of f.c.c. crystal structure in our gold nanoparticles with a good agreement in between the different planes groups and with the bulk lattice constant. As shown in **Figures 8,9** the signal intensities of the peaks are smaller than what we expected, being all smaller than the silica substrate peaks. The background noise is not negligible for at least two peaks ((200) and (222)), at the same time the fit seems to be reliable also in these not ideal conditions. In fact the size values of (111) and (222) peaks, which are parallel families of planes, are in good agreement.

Observing the results of the different size calculation in **Table 5** it can be seen the trend:

$$D_V(200) \leq D_V(220) \simeq D_V(113) \leq D_V(111) \simeq D_V(222)$$

that can suggest a different elongation of the nanoparticles in the various planes direction since when deposited on a solid substrate nanoparticles tend to set on specific positions concerning also crystalline planes for stability, and we can observe this effect with XRD analysis.

For the final radius estimation we computed the weighted mean on the errors of the five peaks for both D'_{VFWHM} and D''_{VFWHM} , obtaining:

$$\begin{aligned}\overline{R'_{VFWHM}} &= 5.05 \pm 0.05\text{nm} \\ \overline{R''_{VFWHM}} &= 6.61 \pm 0.09\text{nm}\end{aligned}$$

The difference between the two methods is the importance given to the contribution of β_{inst} to the final value of β_{obs} . As the size of the nanoparticles is evaluated bigger as the broadening diminishes, a bigger contribution of the instrumental broadening has the effect of measuring bigger nanoparticles. Moreover if we give more reliability to the peak with the higher statistic the resulting radii are

$$\begin{aligned}R'_{VFWHM}(111) &= 6.02 \pm 0.08\text{nm} \\ R''_{VFWHM}(111) &= 8.8 \pm 0.2\text{nm}\end{aligned}$$

4. Scanning Electron Microscopy

The last measurement is done on the same sample used during the previous X-Ray diffraction analysis, by using a Scanning Electron Microscope. In this way we obtain digital images of the gold nanoparticles from which we can extract in a direct way more reliable values of the quantities

of interest, as the size and the shape of the nanoparticles.

A scanning electron microscope (SEM) is an electro-optical instrument with a typical resolution of 1 nm which uses an electron beam to scan the surface and to create an image, by exploiting the scattering of these electrons on the surface of Au nanoparticles and Silica, collecting secondary electrons, back-scattered electrons and X-Rays.

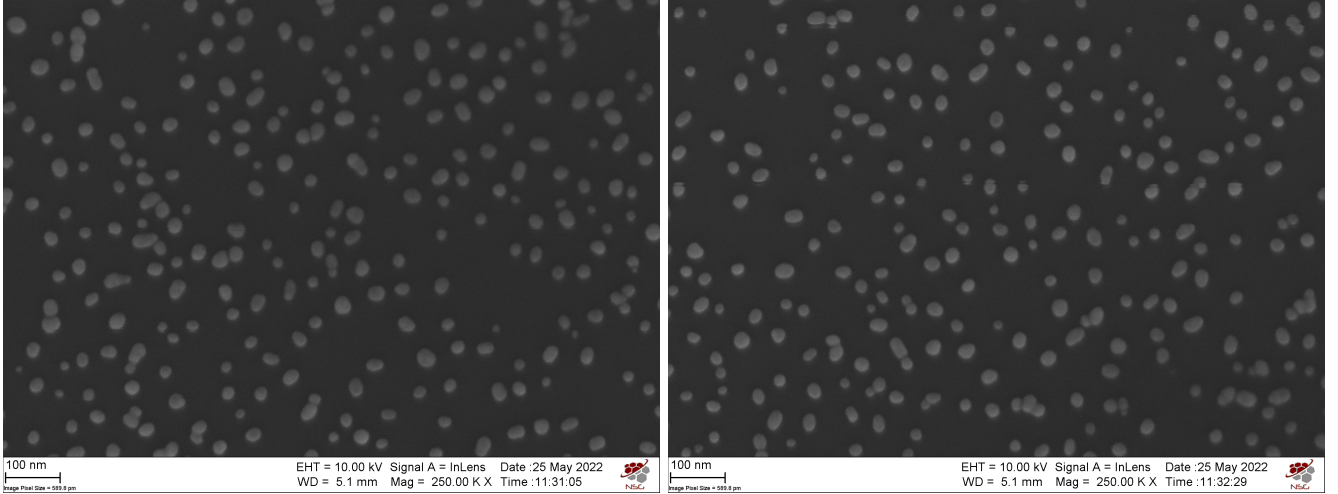


Figure 10: Images acquired by Scanning Electron Microscope.

The SEM images are analyzed through the software *Image J*, adjusting the right resolution of each image by using the information on the pixel image size, and paying attention to exclude nanoparticles at the boundary of the image, which are not totally visualized in the images and can carry incomplete information to the analysis, and aggregates which can alter the size and the shape results. For each image, the measures of surface area A , major and minor axis a_1, a_2 and other informations about the shape of the nanoparticles are collected for each particle, in order to obtain an estimate of the effective radius $R_{eff} = \sqrt{\frac{A}{\pi}}$ and of the aspect ratio $AR = \frac{a_1}{a_2}$, and to understand how much is the approximation of spherical particles reliable.

We thus make an histogram of the effective radius R_{eff} and we fit it with a lognormal probability density function:

$$f(r, A, \mu, \sigma) = \frac{A}{r\sigma\sqrt{2\pi}} e^{-\frac{(ln(r)-\mu)^2}{2\sigma^2}}$$

where A , μ and σ are the fit parameters. We evaluate the mean of the distribution as $\langle R_{eff} \rangle = e^{\mu + \frac{\sigma^2}{2}}$ and, in order to compare the SEM results with the previous ones in which we computed the mean values of the radius by means of volumetric informations, we first evaluate the third moment of the distribution $\langle R_{eff}^3 \rangle = e^{3\mu + \frac{9\sigma^2}{2}}$ and then we take the cubic root $\sqrt[3]{\langle R_{eff}^3 \rangle}$.

We also make an histogram of the eccentricity calculated as $c = \sqrt{1 - (\frac{a_2}{a_1})^2}$ with $a_1 > a_2 = a_3$ and of the aspect ratio AR, which better explicates the correlation between major and minor axis, in order to verify if they shows extreme values, to study the behaviour of their distributions and of the dispersion around the mean value. We therefore make a gaussian fit of the eccentricity histogram, and we extract from it the average eccentricity. This last value will be useful to improve the agreement between theoretical and experimental results, implementing shape corrections in the theory for ellipsoidal nanoparticles. In order to study these corrections, since the analysis is done on 2D images, we suppose to have prolate ellipsoidal nanoparticles, hence with the third axis a_3 equal to the minor axis a_2 .

We repeat the analysis for different data sets. At first we analyze individually the different data set extracted from each SEM image, since different images have different resolutions, hence different error on the measurements. In this way we should be able to estimate the effective radius by reducing the error given by the different image resolutions. However we obtain histograms with strong variations between the different bins, which indicate that the statistics are not sufficient to obtain significant values. Then we make the analysis joining all the measures of the different SEM images together taking into account all the particles, even the correlated ones, i.e. by considering them even if they appear in more than one image in order to obtain an average analysis on the single image having a greater statistics which improves the global error. However in this way the risk is that of statistically overestimating a portion of samples compared to others. At the end we sample images that are not relative to the same magnifications, paying attention to do not consider correlated particles.

The last analysis on the uncorrelated set of particles is the one which gives the best results and thus it is the one on which we perform the fits to extract parameters and expectation values. In the following we report the histogram of the effective radius with the associated lognormal distribution fit in **Figure 11**, the eccentricity histogram with associated gaussian fit in **12**, and the AR histogram in **Figure 13**; following, the fit results of the uncorrelated analysis are reported in **Table 7**, together with the parameters of the lognormal fit in **Table 6**. All the errors on the measures are obtained by propagation.

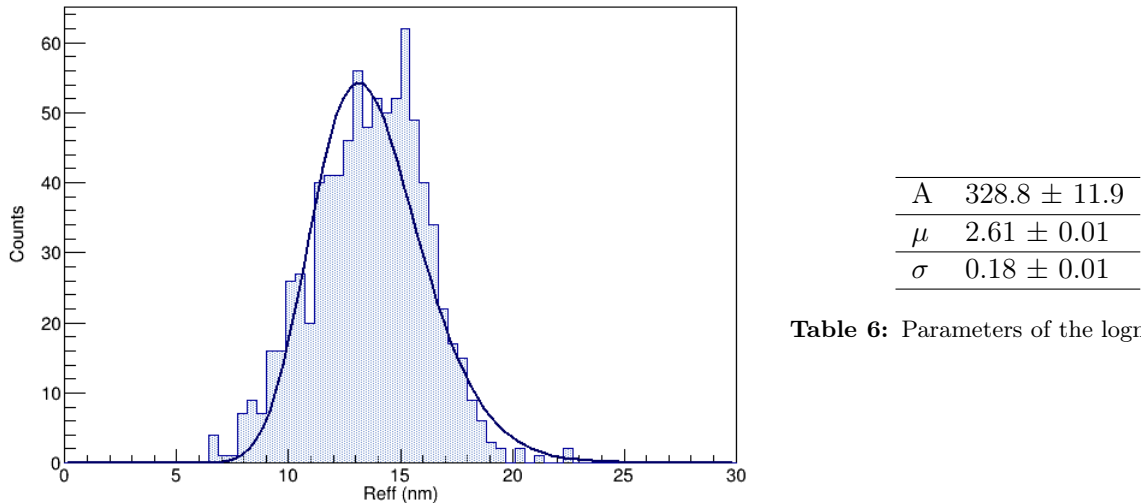


Table 6: Parameters of the lognormal fit.

Figure 11: Histogram of the effective radius R_{eff} with a lognormal distribution fit.

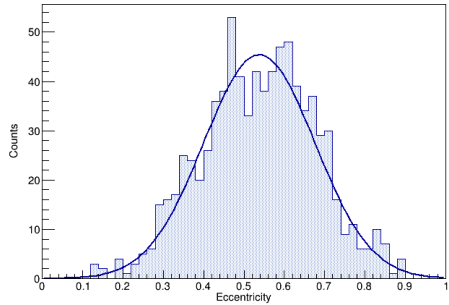


Figure 12: Eccentricity histogram with a gaussian fit, from which the mean value of eccentricity has been extracted.

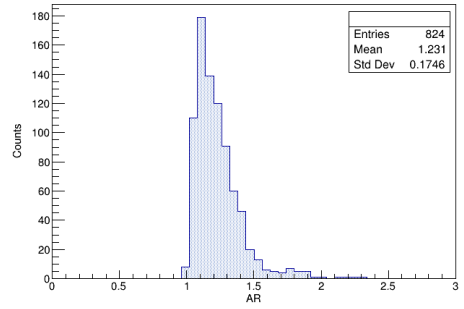


Figure 13: Aspect ratio histogram. In the legend are reported the number of entries, the mean value and the standard deviation.

Number of NP N	Average effective radius $\langle R \rangle$ (nm)	Volume-averaged effective radius $\sqrt[3]{\langle R^3 \rangle}$ (nm)	Average eccentricity e	Aspect ratio AR
824	13.8 ± 0.1	14.3 ± 0.1	0.538 ± 0.006	1.231

Table 7: SEM values calculated with the sample of uncorrelated nanoparticles.

4.1. Comments

Looking at **Figure 11** we observe that the theoretical lognormal density function does not fit well the experimental histogram of R_{eff} , especially for low values of the effective radius, and the histogram looks more like a mirrored lognormal distribution. This is somewhat expected, since we can see from the SEM images that there were lots of aggregates nanoparticles, perhaps due to an inhomogeneous deposit of the Au solution on the silicon sample. During the analysis with the software ImageJ it has been difficult to recognize such type of nanoparticle, even with a suitable value of size threshold, and many of these aggregates were included in the data analysis. An additional source of error to take into account is the trial-and-error method used to set the color threshold in the analysis software to recognize the shape and the size of the nanoparticles, which can affect the extreme values of the effective radius distribution.

These observations are not just affecting the size of the nanoparticles, but also their shape, as it is reflected by the histograms of the eccentricity (**Figure 12**) and by the aspect ratio (**Figure 13**), which show non negligible values of both values, indicating an incorrectness in the hypothesis of spherical nanoparticles. In the first one we see that a gaussian fit is in enough agreement with the shape of the histogram. The fact that the eccentricity values of the nanoparticles are normal distributed, and that the dispersion around the mean value is quite large, ensure us on the reliability of the analysis and of the used sample of nanoparticles, so that a simple shape correction in the theoretical hypothesis by using the average eccentricity value should be sufficient to get best agreement with the experimental results. In the histogram of AR we see again that in average the particles shape slightly deviates from the spherical one, and this is shown particularly by the histogram tail for events with high aspect ratio, highlighting the not exactly spherical shape of the nanoparticles and the inclusion of elongated aggregates in the analysis.

5. Shape correction

In **paragraph 4** we discussed that the shape of the nanoparticles is not exactly spherical and therefore the hypothesis of spherical particles is incorrect. We can therefore consider a correction for the shape of the nanoparticles using the Gans theory which considers ellipsoidal nanoparticles. The extinction cross section σ_{ext} is given by the following formula:

$$\sigma_{ext} = \frac{1}{3} \frac{2\pi}{\lambda} \varepsilon_m^{3/2} \frac{4}{3} \pi R^3 \sum_{j=1}^3 \frac{\varepsilon_2/L_j^2}{[\varepsilon_1 + \varepsilon_m(1 - L_j)/L_j]^2 + \varepsilon_2^2}$$

Where L_j are the polarization coefficients. Considering the shape of prolate ellipsoids, the coefficients L_j are:

$$L_1 = \frac{1-e^2}{e^2} \left[\frac{1}{2e} \ln \frac{1+e}{1-e} - 1 \right]$$

$$L_2 = L_3 = \frac{1-L_1}{2}$$

where e is the eccentricity shown in **Table 7**. We consider the expression for the absorbance with the size correction and this shape correction and we found the values of (R, ρ, ε_m) for which χ^2 is minimum using a triple cycle as explained in **paragraph 1**. The results obtained are shown in **Table 8**.

$R(\text{nm})$	$\rho(\text{nm}^{-3})$	ε_m	χ^2
4.8 ± 0.2	$(5 \pm 1) \cdot 10^{-11}$	1.9 ± 0.2	0.0205023

Table 8: The values of R , ρ and ε_m with the size correction and the shape correction.

With this correction there is a better reliability because the χ^2 is smaller than in **Table 3**. The **Figure 14** shows the absorbances of **Figure 7** with also the absorbance $A_{sc,el}(R, \rho, \varepsilon_m)$ obtained with the shape correction. As can be seen from the **Table 8** the value of the radius has increased and for this reason the curve $A_{sc,el}(R, \rho, \varepsilon_m)$ is slightly closer to the A_{exp} curve in the interband region than $A_{sc}(R, \rho, \varepsilon_m)$ is. We also have a better result for the value of ε_m because now the refractive index is $n \simeq 1.40$ which is closer to the refractive index of water than the refractive index obtained in **paragraph 1**.

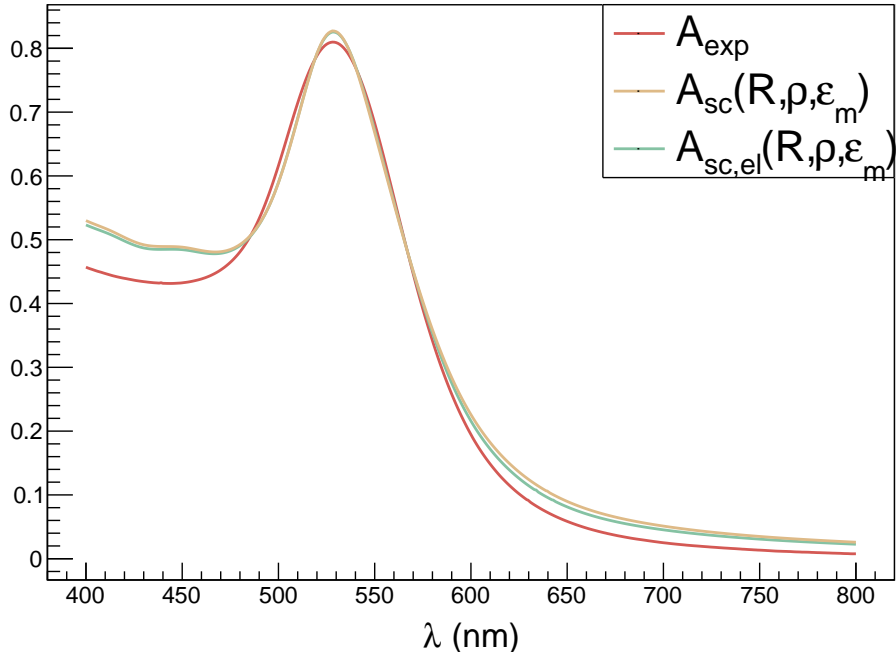


Figure 14: The experimental absorbance A_{exp} , the Absorbance A_{sc} obtained in optical spectroscopy and the absorbance $A_{sc,el}$ with size and shape correction.

6. Conclusion

We calculated various parameters of a sample of gold nanoparticles with three different analysis approaches. Optical spectroscopy (OS) and X-ray diffraction (XRD) investigated the sample by studying the effects produced by the interaction of a photons' beam in different regimes (visible light and X-rays). They gave reliable measures of parameters as the refractive index of water $n = \sqrt{\epsilon_m}$ and the lattice parameter a , comparable to known ones. Scattering electron microscopy (SEM) gave us a direct visible measure of the particles sizes and shapes, but of a limited portion of the whole particles population. Our mean of comparison between the three methods was the mean radius of the nanoparticles, as shown in **Table 9**:

Method		Radius (nm)
OS	R_{Mie}	4.0 ± 0.2
	R_{Gans}	4.8 ± 0.2
XRD	\overline{R}'_{VFWHM}	5.05 ± 0.05
	\overline{R}''_{VFWHM}	6.61 ± 0.09
	$R'_{VFWHM}(111)$	6.02 ± 0.08
	$R''_{VFWHM}(111)$	8.8 ± 0.2
SEM	$\langle R \rangle$	13.8 ± 0.1
	$\sqrt[3]{\langle R^3 \rangle}$	14.3 ± 0.1

Table 9: Main size results of the different methods of analysis.

We note that the first two values of the nanoparticles radius, obtained from Optical Spectroscopy and XRD, are comparable, while the third value, obtained from SEM, differs significantly. Keeping as reference the mean volumetric value of the radius obtained from the SEM, since it has been obtained through a direct measurement of the nanoparticles, we note that the radius value obtained in XRD from the (111) peak with the second method of calculation of β_{size} is comparable with the SEM one, considering also that the SEM value could be overestimated due to the inclusion of agglomerates in the analysis and that the nanoparticles can be composed by different crystallites domains, underestimating their size with the XRD measure. About the OS value of the radius, it increases by introducing the Gans theory, but it is still different respect to other two measures. However, all the results are of the same order of magnitude, ensuring us to have obtained a meaningful characterization of the Au nanoparticles.